Optical absorption spectra of metal oxides from time-dependent density functional theory and many-body perturbation theory based on optimally-tuned hybrid functionals

Guy Ohad,[1,*] Stephen E. Gant,[2,3,*] Dahvyd Wing,[1] Jonah B. Haber,[2,3] María Camarasa-Gómez,[1] Francisca Sagredo,[2,3] Marina R. Filip,[4] Jeffrey B. Neaton,[2,3,5] and Leeor Kronik[1]

[1]*Department of Molecular Chemistry and Materials Science, Weizmann Institute of Science, Rehovoth 76100, Israel*
[2]*Department of Physics, University of California, Berkeley, Berkeley, California 94720, USA*
[3]*Materials Sciences Division, Lawrence Berkeley National Laboratory, Berkeley, California 94720, USA*
[4]*Department of Physics, University of Oxford, Oxford OX1 3PJ, United Kingdom*
[5]*Kavli Energy NanoSciences Institute at Berkeley, University of California, Berkeley, Berkeley, California 94720, USA*

(Received 30 August 2023; revised 27 October 2023; accepted 8 November 2023; published 5 December 2023)

Using both time-dependent density functional theory (TDDFT) and the "single-shot" GW plus Bethe-Salpeter equation (GW-BSE) approach, we compute optical band gaps and optical absorption spectra from first principles for eight common binary and ternary closed-shell metal oxides (MgO, Al_2O_3, CaO, TiO_2, Cu_2O, ZnO, $BaSnO_3$, and $BiVO_4$), based on the nonempirical Wannier-localization-based, optimally tuned, screened range-separated hybrid functional. Overall, we find excellent agreement between our TDDFT and GW-BSE results and experiment, with a mean absolute error smaller than 0.4 eV, including for Cu_2O and ZnO that are traditionally considered to be challenging for both methods.

DOI: 10.1103/PhysRevMaterials.7.123803

I. INTRODUCTION

The optical absorption spectrum is a solid-state property of critical importance in optoelectronic materials. A state-of-the-art *ab-initio* methodology for predicting accurate optical spectra of solids is the GW plus Bethe-Salpeter equation (BSE) approach, where G is the single-particle Green's function and W is the dynamically screened Coulomb interaction [1–5]. The accuracy of GW-BSE calculations comes at a computational cost that in practice scales roughly as N^4, where N is the number of atoms in the system. Time-dependent density functional theory (TDDFT) [6–10] can be an attractive alternative due to its reduced computational cost [3]. However, it suffers from serious inaccuracies when applied to the solid state using standard exchange-correlation functionals [9,11].

Excited-state properties of solids from linear-response TDDFT are typically obtained by solving the Casida equation based on Kohn-Sham (KS) orbitals [12]. The adiabatic approximation is typically employed, by using the ground-state KS approximation for the exchange-correlation potential, V_{xc}, to obtain the exchange-correlation kernel, f_{xc}, defined as the functional derivative of V_{xc} with respect to the electron density. This kernel is a key quantity in the Casida equation and highly affects the accuracy of the resulting optical spectra. This is manifested in two major challenges in predicting optical spectra that are in good agreement with experiment and with GW-BSE calculations. First, TDDFT based on KS (semi-)local functionals inherits the underlying KS band gap, which is known to be severely underestimated [3,13]. The resulting optical spectra are then typically redshifted with respect to experiment [3,14–16]. Second, the exchange-correlation kernel derived from (semi-)local functionals lacks the correct long-wavelength limit, namely, $f_{xc}(q \to 0) \propto 1/q^2$ (where q is a reciprocal space vector in the Brillouin zone), which is an essential property for an accurate description of excitonic effects [7,10,17,18]. Using (semi-)local approximations for optical spectra calculations then results in incorrect line shapes [3,9,14–17].

Within KS TDDFT, several approaches for overcoming these two challenges have been proposed in recent years. In many cases, the two aforementioned challenges are treated separately. The band-gap problem is often solved based on a fit to a target value, e.g., by using a scissors operator to correct the eigenvalues [19]. Subsequently, several ideas have been put forth for constructing a kernel that recovers the correct long-wavelength limit (see Refs. [9,10] and references therein). While good results can be obtained using such methods, they can be computationally complex, and usually at least one of the aforementioned challenges is solved empirically, limiting the predictive power of these methods. Therefore a broader, nonempirical and simple formalism that can solve both challenges at the same time is desirable. We note a recent nonempirical approach proposed by Cavo *et al.* [20], based on the link between the exchange-correlation kernel and the derivative discontinuity. While their approach treats the band-gap problem explicitly, excitonic effects are captured by using the polarization functional within the framework of time-dependent current density-functional theory (DFT).

An alternative approach, still entirely within TDDFT, is based on the use of hybrid functionals within generalized KS (GKS) theory [21–23]. The inclusion of nonlocal effects in GKS, or more specifically, the incorporation of exact exchange in hybrid functionals, has the potential to solve the two fundamental problems described above simultaneously.

*These authors contributed equally to this work.

This is because the free parameters that control the amount of exact (Fock) exchange in a hybrid functional can be chosen such that the band-gap description is improved and the correct long-wavelength limit is accounted for. The latter is achieved by preserving a nonzero fraction of exact exchange in the long range such that the functional possesses the correct asymptotic behavior [24–30] and the kernel behaves as $1/q^2$ in the long-wavelength limit [25,27]. Clearly, a key issue is then how to determine the parameters of a hybrid functional. Importantly, while the formal scaling of GW and hybrid-functional-based DFT is the same, hybrid-functional calculations are faster and more efficient than GW calculations in practice [31,32]. The main differentiator is the high computational cost associated with the explicit construction of the dielectric matrix in GW calculations (see the Methods section below).

Several nonempirical, hybrid-functional-based methods for optical spectra calculations have been proposed in recent years. Yang *et al.* [33] proposed a screened exact-exchange (SXX) approach to replace the full dielectric function in the BSE kernel with a single screening parameter that can be calculated within the random phase approximation (RPA) [5]. Sun *et al.* [34,35] then proposed constructing a hybrid kernel by combining SXX and (semi-)local exchange and correlation kernels. Tal *et al.* [32] used dielectric-dependent hybrid functionals [36], where the parameters are determined self-consistently based on fitting to a dielectric function calculated via the RPA.

A promising hybrid functional in the context of optical spectra calculations is the screened range-separated hybrid (SRSH) functional [25,26], as it has a potential that by construction behaves as $\frac{1}{\varepsilon_\infty r}$ for a large interelectronic distance r, where ε_∞ is the high-frequency dielectric constant of the material. It has been demonstrated repeatedly that when the SRSH parameters are empirically fitted to reproduce the GW or the experimental band gap, one can obtain highly accurate optical absorption spectra of solids [27,37–41].

Recently, we removed the empiricism in SRSH fundamental band-gap calculations in the solid state by choosing the parameters of SRSH based on a Wannier-localized, optimally tuned SRSH (WOT-SRSH) functional [42]. In this method, the range-separation parameter is selected to satisfy an *ansatz* that generalizes the ionization potential theorem to the removal of an electron from a localized Wannier function [43]. This method has been shown to yield highly accurate quasiparticle (QP) band gaps for prototypical semiconductors and insulators [42] and for halide perovskites [44] that are in excellent agreement with experimental and GW results. Furthermore, the merit of using an optimally tuned eigensystem as a starting point to single-shot G_0W_0 calculations has been recently demonstrated by Gant *et al.* [45], who obtained highly accurate band gaps, band widths and d-band locations for a variety of semiconductors. They further showed that WOT-SRSH, both by itself and as a starting point to single-shot G_0W_0, outperforms other hybrid-functional starting points and even quasiparticle self-consistent GW. In light of this success and based on the accuracy of the prior empirical SRSH calculations discussed above, it is evident that WOT-SRSH holds a significant potential for accurate, nonempirical optical spectra predictions for solids.

An interesting application is the case of metal oxides (MOs), which are of much importance in various applications, including solar cells, catalysts, batteries, and sensors [46,47]. From a computational perspective, the accurate prediction of the electronic structure and optical properties of MOs is challenging and has been widely studied (see, e.g., Refs. [48–69]). The major challenges with MOs are attributed to the localized nature of the electrons in the d orbitals. The well-known one-electron self-interaction error [30,70] and delocalization error (or deviation from piecewise linearity) [30,71] associated with (semi-)local functionals are more significant for MOs, leading to DFT calculations that predict unphysical metallic behavior for some systems [51,52,55]. Promisingly, the fraction of exact exchange employed in hybrid functionals directly reduces these errors and has been shown to offer a better description of their electronic structure [48–52,55].

In this article, we assess the accuracy of the WOT-SRSH method in predicting the optical absorption spectra of a set of MO crystals. We perform both TDDFT and GW-BSE calculations for eight common binary and ternary closed-shell MOs, using the WOT-SRSH formalism as a nonempirical foundation for both sets of calculations. We find that both methods agree well with one another and predict optical absorption spectra in good agreement with experiment. Our calculations demonstrate the applicability of WOT-SRSH to complex systems, either in itself, using TDDFT, or as a starting point for GW-BSE calculations.

II. METHODS

A. Materials

We focus on eight abundant closed-shell metal oxides for which both computational and experimental data is available in the literature: MgO, Al_2O_3, CaO, TiO_2, Cu_2O, ZnO, $BaSnO_3$ [72], and $BiVO_4$ [73]. To ensure consistency with experimental results, we use experimental crystal structures at room temperature, the details of which are given in Table I.

B. DFT

1. WOT-SRSH

The SRSH functional [26] splits the Coulomb operator via the identity

$$\frac{1}{|\boldsymbol{r}-\boldsymbol{r}'|} = \underbrace{\alpha\frac{\mathrm{erfc}(\gamma|\boldsymbol{r}-\boldsymbol{r}'|)}{|\boldsymbol{r}-\boldsymbol{r}'|}}_{\text{xx, SR}} + \underbrace{(1-\alpha)\frac{\mathrm{erfc}(\gamma|\boldsymbol{r}-\boldsymbol{r}'|)}{|\boldsymbol{r}-\boldsymbol{r}'|}}_{\text{KSx, SR}} + \underbrace{\varepsilon_\infty^{-1}\frac{\mathrm{erf}(\gamma|\boldsymbol{r}-\boldsymbol{r}'|)}{|\boldsymbol{r}-\boldsymbol{r}'|}}_{\text{xx, LR}} + \underbrace{\left(1-\varepsilon_\infty^{-1}\right)\frac{\mathrm{erf}(\gamma|\boldsymbol{r}-\boldsymbol{r}'|)}{|\boldsymbol{r}-\boldsymbol{r}'|}}_{\text{KSx, LR}}, \tag{1}$$

where the exchange expressions that result from the four terms are evaluated with exact-exchange (xx) integrals for the first and third terms and with semilocal Kohn-Sham exchange (KSx) integrals (in this work, the Perdew-Burke-Ernzerhof, PBE, functional [81]) for the second and fourth terms. In this construct, the fraction of exact exchange in the short range (SR) is α and the fraction of exact exchange in the long range (LR) is the inverse of the dielectric constant, ε_∞^{-1}. In this

TABLE I. Structural details of the crystals used in the calculations.

	Crystal structure	Space group	Unit-cell parameters (Å)
MgO[a]	Rocksalt	Fm-3m	$a = b = c = 4.22$
Al_2O_3[b]	Corundum	R-3cH	$a = b = 4.76, c = 13.00$
CaO[a]	Rocksalt	Fm-3m	$a = b = c = 4.81$
TiO_2[c]	Rutile	$P42/mnm$	$a = b = 4.59, c = 2.96$
Cu_2O[d]	Cubic	Pn-3mZ	$a = b = c = 4.27$
ZnO[e]	Wurtzite	$P63mc$	$a = b = 3.25, c = 5.21$
$BaSnO_3$[f]	Perovskite	Pm-3m	$a = b = c = 4.11$
$BiVO_4$[g]	Monoclinic	$C2/c$	$a = b = 6.88, c = 5.09$
			$\alpha = 68.45^\circ, \beta = 111.55^\circ, \gamma = 63.56^\circ$

[a]Reference [74]; [b]Reference [75]; [c]Reference [76]; [d]Reference [77]; [e]Reference [78]; [f]Reference [79]; [g]Reference [80].

manner, a different balance between exchange and correlation is obtained in the SR and LR, the transition between which is controlled by the range-separation parameter, γ. The default choice for α is 0.25, adopted from the hybrid Perdew-Burke-Ernzerhof (PBE0) [82,83] and the Heyd-Scuseria-Ernzerhof (HSE06) [84] functionals, although it may vary based on considerations discussed below. The choice of ε_∞^{-1} as the fraction of exact exchange in the LR attains the asymptotically correct potential of the SRSH functional [24–30].

The procedure of selecting γ is often carried out in a nonempirical fashion by enforcing an exact physical condition, the ionization potential theorem (IPT) [85–88]. This procedure, known as optimal tuning, has shown great success in the prediction of fundamental gaps of molecules [89–96]. In the bulk limit, however, optimal tuning fails because the IPT is trivially satisfied for every parametrization of SRSH (or indeed any functional) [71,97–99], such that the uniqueness of the optimally-tuned γ that is achieved in molecules is lost.

The reason for the failure of optimal tuning in the bulk limit is the natural delocalization of the electronic orbitals. Recently, a number of studies have exploited different localization schemes for electronic structure predictions [43,57,100–114]. Similarly, the WOT-SRSH approach adopts a criterion that generalizes the IPT to the removal of charge from a maximally localized Wannier function [42]. This *ansatz*, inspired by Ma and Wang [43], is given by

$$\Delta I^\gamma = E^\gamma_{\text{constr}}[\phi](N-1) - E^\gamma(N) + \langle\phi|\,\hat{H}^\gamma_{\text{SRSH}}\,|\phi\rangle = 0, \tag{2}$$

where $E^\gamma(N)$ is the total energy of the system with N electrons and $E^\gamma_{\text{constr}}[\phi](N-1)$ is the total energy of a system with one electron removed from a Wannier function ϕ, including an image charge correction (see Supplemental Material, SM [115], for further details). $\langle\phi|\,\hat{H}^\gamma_{\text{SRSH}}\,|\phi\rangle$ is the expectation value for the energy of the Wannier function with respect to the SRSH Hamiltonian of an N electron system. The energy of the charged system is calculated under a constraint that allows one to control the occupation of the Wannier function via the Lagrange multiplier λ [42]. The constraint is imposed using the equation

$$\hat{H}_{\text{SRSH}}\,|\psi_i\rangle + \lambda\,|\phi\rangle\,\langle\phi|\psi_i\rangle = \epsilon_i\,|\psi_i\rangle\,, \tag{3}$$

where $\{\psi_i\}$ and $\{\epsilon_i\}$ are the GKS eigenfunctions and eigenvalues, respectively, of the constrained $(N-1)$-electron system.

Here, the WOT-SRSH procedure is carried out in an iterative manner based on the four-step scheme suggested by Wing *et al.* [42]. In step 1 the orientationally averaged ion-clamped dielectric constant, ε_∞, is calculated in the primitive unit cell. In step 2 we compose maximally localized Wannier functions from the topmost valence bands in a supercell. We then select the Wannier function with highest energy in the manifold and use it in step 3, where we enforce the *ansatz* given in Eq. (2) by selecting the range-separation parameter γ so that $\Delta I^\gamma = 0$ for the supercell. Finally, in step 4 we calculate properties of interest with the selected γ. This scheme is repeated iteratively: ε_∞ in step 1 is initially calculated using HSE06, and after performing steps 2–4, ε_∞ is calculated again using the optimally-tuned parameters found in step 3.

In the scheme described above, α is kept fixed. As can be seen in Table II, we do not always use the default choice of 0.25. There are two scenarios where α has to be changed, already encountered in previous WOT-SRSH studies [42,44]. The first scenario is that the fraction of LR exact exchange, ε_∞^{-1}, is close to 0.25, resulting in the insensitivity of ΔI to variations in γ. The second scenario is that there is no γ for which the generalized IPT is satisfied. In this work these two issues are solved by increasing α from the default value in three of the materials. An additional criterion in the selection of α is that the functional exhibit the full asymptotic ε_∞^{-1} behavior within the supercell. This is ensured by demanding that $\text{erf}(\gamma^* r_{\text{max}}) \approx 1$, where γ^* is the optimally-tuned range-separation parameter for the chosen α and r_{max} is the maximal distance between two electrons in the supercell. We note that, as demonstrated in Ref. [42], the QP band gap from WOT-SRSH is somewhat sensitive to the choice of α. This sensitivity is reduced when using G_0W_0 based on a WOT-SRSH starting point [45].

TABLE II. Self-consistent WOT-SRSH parameters obtained in this work. ε_∞ is orientationally averaged.

	α	ε_∞	γ (Å^{-1})
MgO	0.25	2.85	2.40
Al_2O_3	0.40	2.94	1.40
CaO	0.25	3.25	1.70
TiO_2	0.25	6.25	0.85
Cu_2O	0.25	6.51	0.95
ZnO	0.30	3.57	1.30
$BaSnO_3$	0.30	3.92	1.40
$BiVO_4$	0.25	5.92	2.00

We emphasize that while the parameters α, ε_∞, and γ are system dependent, they are nonempirical. The self-consistent WOT-SRSH parameters used in this work are reported in Table II. They have been obtained for QP band-gap convergence to within 50 meV, a condition achieved with up to three iterations. See the SM [115] for additional computational details.

2. TDDFT

Optical spectra are computed using linear-response TDDFT by solving the Casida equation within the Tamm-Dancoff approximation [7,116]. The Casida equation then has the following form [12,22,27,117]:

$$\Omega^S A^S_{vc\boldsymbol{k}} = \left(\epsilon^{\mathrm{GKS}}_{c\boldsymbol{k}} - \epsilon^{\mathrm{GKS}}_{v\boldsymbol{k}}\right)A^S_{vc\boldsymbol{k}} + \sum_{v'c'\boldsymbol{k}'}\big[\langle v\boldsymbol{k}, c\boldsymbol{k}|K_{Hxc}(\alpha,\varepsilon_\infty,\gamma)|v'\boldsymbol{k}', c'\boldsymbol{k}'\rangle - \langle v\boldsymbol{k}, v'\boldsymbol{k}'|K_{\mathrm{sxx}}(\alpha,\varepsilon_\infty,\gamma)|c\boldsymbol{k}, c'\boldsymbol{k}'\rangle\big]A^S_{v'c'\boldsymbol{k}'}, \quad (4)$$

where v and c denote valence- and conduction-band states, respectively, ϵ^{GKS} are the GKS eigenvalues, Ω^S are the excitation energies, and $A^S_{vc\boldsymbol{k}}$ are the expansion coefficients of the exciton wave function Ψ_S in terms of valence- and conduction-band-state pairs at the same $\boldsymbol{k}$ point, namely,

$$\Psi_S(\boldsymbol{r}_e, \boldsymbol{r}_h) = \sum_{vc\boldsymbol{k}} A^S_{vc\boldsymbol{k}}\psi_{c\boldsymbol{k}}(\boldsymbol{r}_e)\psi^*_{v\boldsymbol{k}}(\boldsymbol{r}_h). \quad (5)$$

As expressed in Eq. (4), the TDDFT kernel is composed of two parts: the Hartree-exchange-correlation kernel, K_{Hxc}, and the screened exact-exchange kernel K_{sxx}, defined as

$$K_{Hxc}(\alpha,\varepsilon_\infty,\gamma) = \frac{1}{|\boldsymbol{r}-\boldsymbol{r}'|} + (1-\alpha)f^{\mathrm{SR},\gamma}_{xc} + \left(1-\varepsilon^{-1}_\infty\right)f^{\mathrm{LR},\gamma}_{xc} \quad (6)$$

and

$$K_{\mathrm{sxx}}(\alpha,\varepsilon_\infty,\gamma) = \alpha\frac{\mathrm{erfc}(\gamma|\boldsymbol{r}-\boldsymbol{r}'|)}{|\boldsymbol{r}-\boldsymbol{r}'|} + \varepsilon^{-1}_\infty\frac{\mathrm{erf}(\gamma|\boldsymbol{r}-\boldsymbol{r}'|)}{|\boldsymbol{r}-\boldsymbol{r}'|}, \quad (7)$$

where $f^{\mathrm{SR},\gamma}_{xc}$ and $f^{\mathrm{LR},\gamma}_{xc}$ are the short- and long-range contributions, respectively, of the exchange-correlation kernel of the (semi-)local Kohn-Sham approximation. The bracket notation in Eq. (4) represents real space integrals of the form

$$\langle b_1\boldsymbol{k}_1, b_2\boldsymbol{k}_2|K|b_3\boldsymbol{k}_3, b_4\boldsymbol{k}_4\rangle = \int d^3r d^3r'\psi^*_{b_1\boldsymbol{k}_1}(\boldsymbol{r})\psi_{b_2\boldsymbol{k}_2}(\boldsymbol{r})K(\boldsymbol{r},\boldsymbol{r}')\psi_{b_3\boldsymbol{k}_3}(\boldsymbol{r}')\psi^*_{b_4\boldsymbol{k}_4}(\boldsymbol{r}'), \quad (8)$$

where b_i can be a valence- or conduction-band index, and it is understood that the wave functions on the left-hand side always have position $\boldsymbol{r}$ and the wave functions on the right-hand side always have position $\boldsymbol{r}'$.

Once the linear-response equation is solved, optical absorption spectra (i.e., the imaginary part of the dielectric function, ε_2) can be obtained by

$$\varepsilon_2(\omega) = \frac{16\pi^2}{\omega^2}\sum_S|\hat{\boldsymbol{p}}\cdot\langle 0|\mathbf{v}|S\rangle|^2\delta(\omega-\Omega^S), \quad (9)$$

where

$$\langle 0|\mathbf{v}|S\rangle = \sum_{vc\boldsymbol{k}} A^S_{vc\boldsymbol{k}}\,\langle v\boldsymbol{k}|\mathbf{v}|c\boldsymbol{k}\rangle\,, \quad (10)$$

S is a neutral excitation, $\mathbf{v}$ is the single-particle velocity operator, and $\hat{\boldsymbol{p}}$ is the direction of the polarization of light.

TDDFT calculations in this work are performed at both the PBE level (denoted TDPBE), the equation for which is obtained by using the PBE eigenvalues and setting $\alpha = \varepsilon^{-1}_\infty = 0$ in Eq. (4), and at the WOT-SRSH level (denoted TDWOT-SRSH), the equation for which is obtained by using the WOT-SRSH eigenvalues and the optimally-tuned α, ε_∞, and γ parameters in Eq. (4). See SM [115] for additional computational details.

C. Many-body perturbation theory

1. GW approximation

Within the framework of many-body perturbation theory (MBPT), the electron self-energy Σ can be approximated to first order as the convolution of G and W, written symbolically as $\Sigma = iGW$ [4]. Σ is usually constructed from an underlying DFT eigensystem, $\{\psi_{n\boldsymbol{k}}, \epsilon^{\mathrm{DFT}}_{n\boldsymbol{k}}\}$, at varying levels of self-consistency, with the choice of self-consistency usually having significant implications for the accuracy and variability of results [5,62–64,66,118–120]. The simplest approach, and the one employed in this work, is the "single-shot" method (denoted G_0W_0), where the QP energies are calculated as a first-order perturbative correction to a DFT eigensystem [3,5,66,121].

Specifically, the single-particle Green's function, G_0, is constructed directly from the DFT eigensystem, and the dynamically screened Coulomb interaction W_0 is given by

$$W_0(\boldsymbol{r},\boldsymbol{r}';\omega) = \int d\boldsymbol{r}''\varepsilon^{-1}(\boldsymbol{r},\boldsymbol{r}'';\omega)\frac{1}{|\boldsymbol{r}'-\boldsymbol{r}''|}, \quad (11)$$

where the dielectric function is computed within the RPA based on the polarizability, $\chi_0(\boldsymbol{r},\boldsymbol{r}',\omega)$, given by the Adler-Wiser expression [122,123].

In practice, $\chi_0(\boldsymbol{r},\boldsymbol{r}',\omega)$ can be evaluated explicitly via a full-frequency (FF) calculation, or approximately modeled using a plasmon-pole model (PPM). In the FF approach, the convolution of G_0 with W_0 is handled via contour deformation [124,125] using explicitly sampled frequencies along the imaginary axis. To mitigate the substantial cost of computing the FF dielectric function, we employ the static subspace approximation [126–130], where $\chi_0(\boldsymbol{r},\boldsymbol{r}',\omega)$ is efficiently but approximately represented using the leading eigenvectors of a low-rank decomposition of the static polarizability $\chi_0(\boldsymbol{r},\boldsymbol{r}',0)$. In the PPM approach, χ_0 is evaluated statically ($\omega = 0$) and extended to finite frequencies via a simplified model [5,131,132]. Here we employ FF calculations for all materials except Cu_2O, where we use the PPM. See SM [115] for further details.

With the above quantities, the G_0W_0 self-energy can be used to correct the DFT eigenvalues perturbatively via

$$\epsilon^{\mathrm{QP}}_{n\boldsymbol{k}} = \epsilon^{\mathrm{DFT}}_{n\boldsymbol{k}} + \langle n\boldsymbol{k}|\Sigma\left(\epsilon^{\mathrm{QP}}_{n\boldsymbol{k}}\right) - V_{xc}|n\boldsymbol{k}\rangle\,. \quad (12)$$

Due to the fact that $\epsilon^{\mathrm{QP}}_{n\boldsymbol{k}}$ in Eq. (12) depends on itself, evaluating this expression can be nontrivial. For FF calculations, $\langle n\boldsymbol{k}|\Sigma(\omega)|n\boldsymbol{k}\rangle$ is accurately known for a range of frequencies, allowing for a solution of Eq. (12). However, if a PPM for the frequency dependence of the screening is used, we employ the common practice of expanding Eq. (12) to first order about $\epsilon_{n\boldsymbol{k}}^{\mathrm{DFT}}$ to evaluate it [133–135].

The single-shot approach has the advantage of being the least computationally demanding GW approach, and, typically, the QP band structures computed within G_0W_0 are in substantially better agreement with experiment than those computed from their underlying DFT functionals [66,136–141]. However, the single-shot approach also suffers from a sensitivity to the starting point, i.e., the (G)KS eigensystem used to construct Σ. Hence, the question of how to choose an appropriate DFT starting point for G_0W_0 calculations has been actively debated [66,138,142–147]. In this work we focus on the WOT-SRSH eigensystem as a starting point for G_0W_0 (denoted G_0W_0@WOT-SRSH), as done in Ref. [45], where it was demonstrated to be highly accurate over a broad range of systems. For the sake of comparison, we also examine results obtained from using PBE as a starting point (denoted G_0W_0@PBE). Additional computational details, including convergence tests, can be found in the SM [115].

2. *Ab initio* BSE method

The *ab initio* Bethe-Salpeter equation, within the Tamm-Dancoff approximation [2,3,148], has a standard form that is very similar to the Casida equation. It can be constructed from Eq. (4) by substituting ϵ^{GKS} with ϵ^{QP}, K_{Hxc} with the bare exchange interaction kernel $K_x = \frac{1}{|\boldsymbol{r}-\boldsymbol{r}'|}$, and K_{sxx} with the static screened direct interaction kernel $K_d = W_0(\boldsymbol{r}, \boldsymbol{r}'; \omega = 0)$ [2,149]. In practice, when constructing K_x and K_d, we interpolate from coarse Γ-centered $\boldsymbol{k}$ grids to fine-shifted $\boldsymbol{k}$ grids, as specified in the SM [115]. After solving the BSE, the exciton wave function and the imaginary part of the dielectric function are obtained from Eqs. (5) and (9), respectively. Additional computational details can be found in the SM [115].

D. Vibrational renormalization of band gaps and optical spectra

To make a meaningful comparison with experimental band gaps and optical spectra, two effects should be taken into account: zero-point renormalization (ZPR) energy and finite temperature fluctuations (FTF). Both are inherently excluded in calculations that use the fixed ion approximation but can have a significant effect on electronic properties [36,42,67–69,72,73,156–165]. These effects can be understood from methods that go beyond static DFT, such as molecular dynamics [73,156] and electron-phonon self-energy approaches [67–69,158–162].

Accurate state-dependent calculations of ZPR and FTF effects are beyond the scope of this work. To account for them, we exploit values from the literature. In the absence of a universal method to calculate or measure these effects, we exploit values obtained based on different methods, the details of which are given in Table III. These renormalization values are used as rigid shifts for the computed optical band gaps and optical absorption spectra.

All values in Table III represent the renormalization of the QP band gap due to electron-phonon interactions, except for the case of $BaSnO_3$, where the value corresponds to renormalization of the optical band gap due to exciton-phonon interactions. By applying the same rigid shift to all features in the optical spectra (including the optical band gap itself),

TABLE III. Vibrational renormalization values, taken from prior literature, used in this work as a rigid shift for the computed band gaps and optical absorption spectra. All values include both the ZPR and FTF effects, except for MgO and CaO, where the values include the ZPR effect alone.

	Thermal renorm. [meV]
MgO	–533[a]
Al_2O_3	–310[b]
CaO	–357[a]
TiO_2	–290[c]
Cu_2O	–210[b]
ZnO	–190[b]
$BaSnO_3$	–367[d]
$BiVO_4$	–920[e]

[a]Reference [162], from nonadiabatic Allen-Heine-Cardona theory.
[b]Reference [69], from nonadiabatic Allen-Heine-Cardona theory. The FTF correction is extracted graphically at 300 K.
[c]Reference [67], from nonadiabatic Allen-Heine-Cardona theory. The FTF correction is extracted graphically at 300 K.
[d]Reference [72], from temperature-dependent optical absorption onset measurements.
[e]Reference [73], from path-integral molecular dynamics at the PBE0 level, including nuclear quantum effects.

we implicitly assume the size of the renormalization [166] of exciton binding energies are negligible relative to the energy scales of interest in this work. To demonstrate the validity of this assumption, we calculated phonon screening corrections to the binding energy of the lowest-lying exciton according to the expression derived in Ref. [166] and found that they are smaller than 0.1 eV. We note, however, that these corrections serve as an approximate lower bound to the exciton binding-energy renormalization, because they are based on a model expression, applicable to 1*s* excitons at 0 K. Thus the validity of our estimates may be more questionable for materials that exhibit significant thermal fluctuations. For more details see the SM [115].

III. RESULTS AND DISCUSSION

Figure 1 shows the optical absorption spectra obtained from TDWOT-SRSH, G_0W_0-BSE@WOT-SRSH, and experiment for all materials studied in this work, except $BiVO_4$, which is discussed separately below. For reference, Fig. 1 also shows spectra from TDPBE and G_0W_0-BSE@PBE. As expected, the PBE-based results are unsatisfactory. TDPBE significantly underestimates the reported measured absorption onset, and the line shapes also deviate significantly from experiment. The G_0W_0-BSE@PBE line shapes are more accurate owing to the correct description of electron-hole interactions in BSE but suffer from a redshifted absorption onset relative to experiment due to the PBE starting point. Most notably, TDWOT-SRSH considerably outperforms G_0W_0-BSE@PBE.

We point out that the line shapes of G_0W_0-BSE@PBE and G_0W_0-BSE@WOT-SRSH are similar, but the spectra

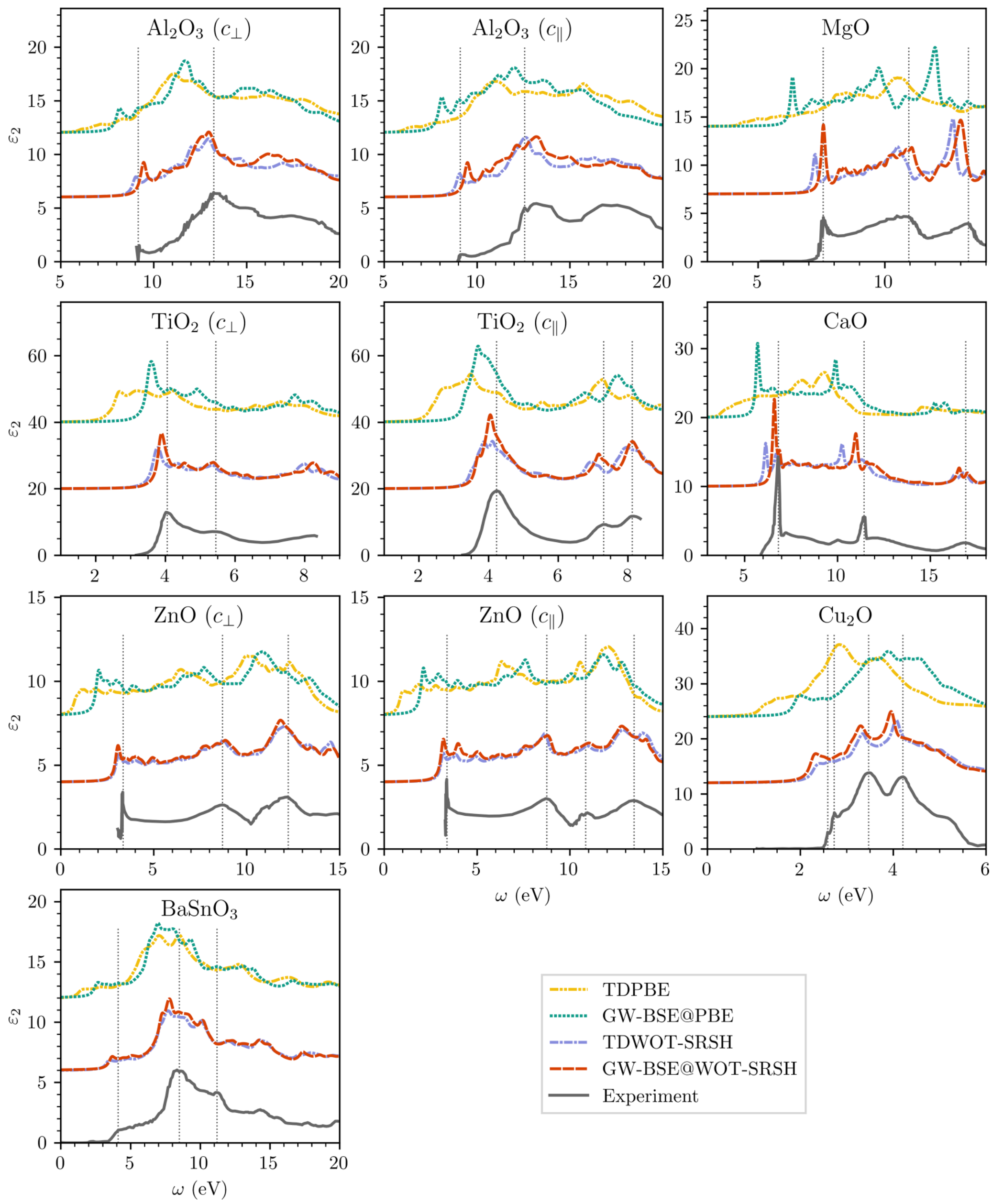

FIG. 1. Imaginary part of the dielectric function, computed with TDPBE (yellow dot-dashed line), G_0W_0-BSE@PBE (green dotted line), TDWOT-SRSH (purple dot-dashed line), and G_0W_0-BSE@WOT-SRSH (red dashed line), compared to experiment (gray solid line). Vertical dotted lines indicate the main spectral features in experiment. The anisotropy in Al_2O_3, TiO_2, and ZnO is accounted for by considering polarization perpendicular to the optic axis (ordinary component, $c_\perp$) and parallel to the optic axis (extraordinary component, $c_\parallel$) explicitly. Computed spectra are rigidly shifted in the energy axis by the vibrational renormalization reported in Table III. They are also shifted in the vertical axis such that the zero absorption tail exactly begins where indicated by an axis tick. Experimental data are taken from the following sources: Al_2O_3: Ref. [150]; MgO: Ref. [151]; TiO_2: Ref. [152]; CaO: Ref. [153]; ZnO: Ref. [154]; Cu_2O: Ref. [155]; and $BaSnO_3$: Ref. [72].

are shifted. This is an indication that the differences result mostly from the one-particle energies being different, while the eigenstates are relatively similar. Generally, significant orbital reordering is known to affect the line shape and not just the absolute position—see, e.g., Ref. [167]. The advantage of using WOT-SRSH over PBE as a starting point is that it leads to a more accurate band gap and band structure, as previously shown in Ref. [45]. We further demonstrate these trends for other starting points of G_0W_0-BSE in the SM [115].

It is readily apparent that both TDWOT-SRSH and G_0W_0-BSE@WOT-SRSH predict peak positions and line shapes in close agreement with each other and with the experimental data. The agreement is consistently good both for the absorption onsets and for higher energy spectral features. Notably, excitonic peak positions are well captured in both methods. In most cases the BSE excitonic peak position is slightly blueshifted compared to the TDDFT one, most notably for Al_2O_3, MgO, and CaO, where the shift is ~0.3–0.4 eV. This shift can be explained primarily at the electronic level, where G_0W_0 corrections tend to blueshift the lowest direct gaps, as seen in the SM [115] and in prior work [45]. This blueshift is largely caused by the underscreening of the Coulomb interaction in W_0, brought about by the use of the RPA in conjunction with an accurate hybrid functional [145,168]. This can be seen when comparing the values of ε_∞ used in WOT-SRSH and the high-frequency RPA dielectric constant (obtained from the same eigensystem) reported in the SM [115]. Relatedly, the underscreening present in W_0 also manifests in an about 10% increase, on average, of the computed G_0W_0-BSE@WOT-SRSH exciton binding energy. This competing effect redshifts the resulting spectra but by much less than the blueshift at the electronic level.

It can be seen that in the three cases where there are larger deviations between the WOT-SRSH-based methods, namely, Al_2O_3, MgO, and CaO, the BSE spectra predict peak positions that are in better overall agreement with experiment, suggesting possible improved predictive accuracy associated with G_0W_0-BSE@WOT-SRSH. However, this improved accuracy can in part be attributed to a cancellation of errors resulting from underscreening, as discussed above.

A notable success of both methods is their accuracy for ZnO, a system known to have significant convergence issues in MBPT that resulted in a range of different reported band-gap values [56,59,62,64,138,142,169–172]. Here, using both WOT-SRSH and G_0W_0@WOT-SRSH, we obtain optical absorption spectra for ZnO in excellent agreement with experiment (after approximately accounting for vibrational effects) and between the two methods without encountering any material-specific difficulties.

Another general trend we observe is that the oscillator strength of the first excitonic peak is reduced in TDDFT compared to BSE, while other features at higher energies are in better agreement. This reflects an underestimation of electron-hole interaction and a more delocalized exciton in TDDFT, in line with previous comparisons between the two methods [37].

For $BiVO_4$, we observe a larger deviation between the WOT-SRSH–based spectra and experiment, as can be seen in Fig. 2. This system was comprehensively studied by Wiktor *et al.* [73], with a special emphasis on the effect of thermal fluctuations on the electronic structure. Excluding these effects and the effect of spin-orbit coupling (which they found to decrease the band gap by only 0.13 eV), they obtained a QP band gap of 3.64 eV using quasiparticle self-consistent GW, in good agreement with our results (3.5 and 3.8 eV from WOT-SRSH and G_0W_0@WOT-SRSH, respectively). Using path-integral molecular dynamics (including nuclear quantum effects) at the PBE0 level, they found a large QP band-gap renormalization of –0.92 eV at 300 K, a value which we adopted in this work. Shifting the QP band gap by this amount brings it very close to the experimental optical indirect band gap of 2.5 eV [173]. While the effect of thermal fluctuations on the QP band gap in $BiVO_4$ has been explored, their effects on the optical absorption spectra, beyond causing a scissor-shift in the electronic bands, has not been studied to the best of our knowledge. Using the aforementioned QP thermal shift in the absorption spectrum may be insufficient for such a complex system with significant thermal fluctuations, because

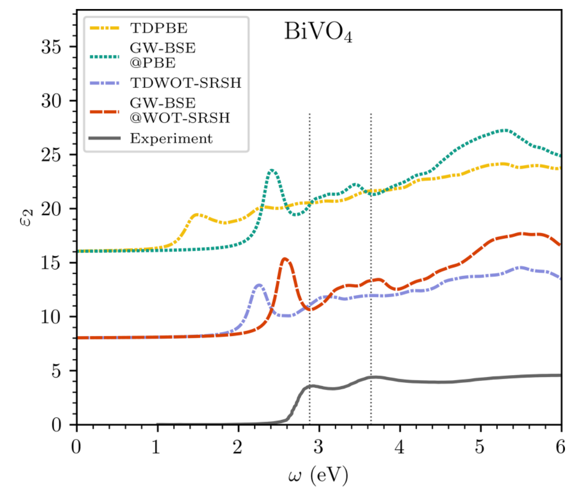

FIG. 2. Same as Fig. 1 but for $BiVO_4$. The anisotropy in the optical response is directionally averaged. Experimental data are taken from Ref. [173].

exciton-phonon interactions may also renormalize the exciton binding energy significantly. We therefore leave the question of thermal effects on the optical properties of $BiVO_4$ for the future, noting the agreement between the WOT-SRSH-based QP band gaps computed in this work and the one obtained by Wiktor *et al.* [73].

Comparing the absorption onset of TDDFT and BSE with experiment in the case of $BaSnO_3$ and $BiVO_4$, we observe sharp excitonic peaks at the onset in both TDDFT and BSE, as opposed to shallow "shoulders" in experiment. This can be directly attributed to significant finite temperature effects in those systems [72,73] that can substantially alter the exciton and reduce the exciton binding energy and oscillator strength of excitonic peaks. These effects are not taken into account in our calculations. We note that peak shapes in agreement with our results have been obtained in Ref. [72] for $BaSnO_3$ and in Ref. [73] for $BiVO_4$ from GW-BSE.

In the context of comparing computed band gaps with experiment, we point out that a comparison of fundamental band gaps with optical experiments is inconsistent for MOs, because the exciton binding energy cannot be neglected. One can, in principle, compare fundamental band gaps with values obtained from, e.g., combined photoemission and inverse photoemission spectroscopy, but such experiments often suffer from significant experimental uncertainties that amount to ~0.4–0.5 eV [174,175] and from sensitivity to surface effects and crystal dynamics [176]. For these reasons, in this work we focus on optical band gaps for the comparison with experiment. Still, as fundamental band gaps are of general interest, we list them in the SM [115].

The optical band gap is defined in most cases in this work as the onset of absorption, where a bright (dipole allowed) excitonic transition can be observed. As our optical spectra calculations do not account for momentum transfer, we choose as a benchmark experimental values that represent minimal direct transitions obtained in optical measurements. Table IV summarizes the optical band gaps predicted from TDWOT-SRSH and G_0W_0-BSE@WOT-SRSH compared to experimental values. The optical-band-gap predictions are

TABLE IV. Computed optical band gaps, compared with experimental optical measurements of direct transitions. Computed values refer to bright excited-state energies at the onset of absorption, unless mentioned otherwise. Corrected values are obtained by adding the vibrational renormalization values taken from Table III. Spin-orbit coupling effects are not included. The mean absolute error (MAE) with respect to experiment is also given. All values are given in electronvolts.

	TDWOT-SRSH	G_0W_0-BSE@WOT-SRSH	Corrected TDWOT-SRSH	Corrected G_0W_0-BSE@WOT-SRSH	Experiment
MgO	7.8	8.1	7.2	7.6	7.7[c]
Al_2O_3	9.3	9.8	9.0	9.4	8.8[d]
CaO	6.5	6.9	6.1	6.6	6.9[c]
TiO_2[a]	3.4	3.6	3.1	3.3	3.0[e]
Cu_2O[b]	2.5	2.4	2.3	2.2	2.6[f]
ZnO	3.2	3.3	3.1	3.1	3.5[g]
$BaSnO_3$	3.8	4.0	3.4	3.6	3.6[h]
$BiVO_4$	3.1	3.5	2.2	2.5	2.7[i]
MAE			0.37	0.31	

[a]Values are dark excitons. See text for additional information.
[b]Values are first bright excited state. See text for additional information.
[c]Reference [177], from thermoreflectance spectra at 85 K.
[d]Reference [178], from VUV reflectance at 300 K.
[e]Reference [179], from absorption spectra at 1.6 K.
[f]Reference [180], from photoluminescence spectra at 6 K.
[g]Reference [181], from wavelength-modulated reflectivity measurements at low temperature.
[h]Reference [72], from electron-energy-loss spectroscopy at 300 K.
[i]Reference [173], from UV-vis absorption spectroscopy.

in overall good agreement between the two methods and experimental values, indicated by mean absolute errors of ~0.3–0.4 eV with respect to experiment. We note that some discrepancies with respect to experimental gaps are to be anticipated, because there can be ambiguity associated with the choice of the model and fitting method used to analyze the absorption edge or the spectral features in experimental data. We also highlight that this work primarily focuses on the optical absorption spectra as a whole, where extrapolation is not needed to make a direct comparison. Additionally, we emphasize that while the shifted fine $\boldsymbol{k}$ grids used to compute the optical absorption spectra are relatively converged with respect to the overall peak positions and line shape in the scale of the plot, the absorption onset obtained from our calculations is likely somewhat underconverged [2,34] (see SM [115] for more details).

There are two exceptional cases to the above definition for the optical band gap. These are rutile TiO_2 and Cu_2O, where the onset of absorption is a dark (dipole forbidden) transition. In TiO_2, the dark bound 1*s* exciton has been resolved by Pascual *et al.* [179], allowing for direct comparison with TDDFT and BSE results. Both methods predict other in-gap brighter transitions, but those are less directly comparable with existing experimental data. Nonetheless, the shape and position of the first absorption peak (near 4 eV) is in good agreement with experiment for both TDWOT-SRSH and GW-BSE@WOT-SRSH.

The second exception to the above definition is Cu_2O, where the in-gap transitions from the topmost valence bands to the lowest conduction band (the so-called yellow/green exciton series) are dipole-forbidden transitions between states of orbital character of 3*d* and 4*s*, respectively. These bound excitons, which have a *p*-like orbital character, occur just below the fundamental band gap [180,182]. Experimentally, these low-energy transitions are found to occur at 2.03 eV (1s exciton) and 2.15 eV (2p exciton) [182,183], whereas we observe the onset at 1.7 eV and 1.8 eV via TDWOT-SRSH and GW-BSE@WOT-SRSH, respectively. However, the so-called blue or violet excitonic series in Cu_2O, associated with transitions from the topmost valence bands to the second-lowest conduction bands, are dipole allowed and manifest as the lowest energy resonant bright transitions that are clearly apparent in the optical spectra. Thus we choose to define the optical band gap as the first of these bright transitions, which is experimentally observed at 2.6 eV [180]. This value is in good agreement with the corresponding first bright transitions obtained in theory (see Table IV).

IV. CONCLUSIONS

We have demonstrated the accuracy of the nonempirical WOT-SRSH functional for the prediction of the optical absorption spectra of MOs, a group of materials known for their computational complexity. By applying a simple, computationally efficient scheme for choosing the parameters of the SRSH functional, we find excellent agreement between TDWOT-SRSH and G_0W_0-BSE@WOT-SRSH, with slightly increased accuracy of the latter relative to experiment. These results suggest that the range of applicability of WOT-SRSH extends beyond computing band gaps of relatively simple semiconductors and insulators. It can be used with predictive accuracy to compute both electronic and optical properties of more challenging, closed-shell MO systems. This work paves the way for the application of WOT-SRSH to the study of more complex MO systems, including MOs with heavier atoms (e.g., Zr- and Hf-based ones) and open-shell MOs.

ACKNOWLEDGMENTS

This work used the Stampede2 supercomputer at the Texas Advanced Computing Center (TACC) at the University of Texas at Austin through allocation DMR190070 from the Advanced Cyberinfrastructure Coordination Ecosystem: Services & Support (ACCESS) program [184], which is supported by National Science Foundation Grants No. 2138259, No. 2138286, No. 2138307, No. 2137603, and No. 2138296. The authors also acknowledge TACC for providing high performance computing (Frontera) resources that have contributed to the research results reported within this paper [185]. M.C.-G. was additionally supported by the Azrieli Foundation through the award of an Azrieli International Postdoctoral Fellowship. M.R.F acknowledges support from the UK Engineering and Physical Sciences Research Council (EPSRC), Grant No. EP/V010840/1. L.K. was additionally supported by the Aryeh and Mintzi Katzman Professorial Chair and the Helen and Martin Kimmel Award for Innovative Investigation.

[1] S. Albrecht, L. Reining, R. Del Sole, and G. Onida, Excitonic effects in the optical properties, Phys. Status Solidi A **170**, 189 (1998).

[2] M. Rohlfing and S. G. Louie, Electron-hole excitations and optical spectra from first principles, Phys. Rev. B **62**, 4927 (2000).

[3] G. Onida, L. Reining, and A. Rubio, Electronic excitations: Density-functional versus many-body Green's-function approaches, Rev. Mod. Phys. **74**, 601 (2002).

[4] L. Hedin, New method for calculating the one-particle Green's function with application to the electron-gas problem, Phys. Rev. **139**, A796 (1965).

[5] M. S. Hybertsen and S. G. Louie, Electron correlation in semiconductors and insulators: Band gaps and quasiparticle energies, Phys. Rev. B **34**, 5390 (1986).

[6] E. Runge and E. K. Gross, Density-functional theory for time-dependent systems, Phys. Rev. Lett. **52**, 997 (1984).

[7] C. A. Ullrich, *Time-Dependent Density-Functional Theory: Concepts and Applications* (Oxford University Press, Oxford, England, 2011).

[8] K. Burke, Perspective on density functional theory, J. Chem. Phys. **136**, 150901 (2012).

[9] N. T. Maitra, Perspective: Fundamental aspects of time-dependent density functional theory, J. Chem. Phys. **144**, 220901 (2016).

[10] Y.-M. Byun, J. Sun, and C. A. Ullrich, Time-dependent density-functional theory for periodic solids: Assessment of excitonic exchange–correlation kernels, Electron. Struct. **2**, 023002 (2020).

[11] V. Gavrilenko and F. Bechstedt, Optical functions of semiconductors beyond density-functional theory and random-phase approximation, Phys. Rev. B **55**, 4343 (1997).

[12] M. E. Casida, in *Recent Advances in Density Functional Methods Part I*, edited by D. P. Chong (World Scientific, Singapore, 1995), Chap. 5, pp. 155–192.

[13] S. Kümmel and L. Kronik, Orbital-dependent density functionals: Theory and applications, Rev. Mod. Phys. **80**, 3 (2008).

[14] S. Botti, F. Sottile, N. Vast, V. Olevano, L. Reining, H.-C. Weissker, A. Rubio, G. Onida, R. Del Sole, and R. Godby, Long-range contribution to the exchange-correlation kernel of time-dependent density functional theory, Phys. Rev. B **69**, 155112 (2004).

[15] S. Botti, A. Fourreau, F. Nguyen, Y.-O. Renault, F. Sottile, and L. Reining, Energy dependence of the exchange-correlation kernel of time-dependent density functional theory: A simple model for solids, Phys. Rev. B **72**, 125203 (2005).

[16] S. Botti, A. Schindlmayr, R. Del Sole, and L. Reining, Time-dependent density-functional theory for extended systems, Rep. Prog. Phys. **70**, 357 (2007).

[17] P. Ghosez, X. Gonze, and R. Godby, Long-wavelength behavior of the exchange-correlation kernel in the Kohn-Sham theory of periodic systems, Phys. Rev. B **56**, 12811 (1997).

[18] L. Reining, V. Olevano, A. Rubio, and G. Onida, Excitonic effects in solids described by time-dependent density-functional theory, Phys. Rev. Lett. **88**, 066404 (2002).

[19] Z. H. Levine and D. C. Allan, Linear optical response in silicon and germanium including self-energy effects, Phys. Rev. Lett. **63**, 1719 (1989).

[20] S. Cavo, J. Berger, and P. Romaniello, Accurate optical spectra of solids from pure time-dependent density functional theory, Phys. Rev. B **101**, 115109 (2020).

[21] A. Seidl, A. Görling, P. Vogl, J. Majewski, and M. Levy, Generalized Kohn-Sham schemes and the band-gap problem, Phys. Rev. B **53**, 3764 (1996).

[22] S. Tretiak and V. Chernyak, Resonant nonlinear polarizabilities in the time-dependent density functional theory, J. Chem. Phys. **119**, 8809 (2003).

[23] R. Baer and L. Kronik, Time-dependent generalized Kohn–Sham theory, Eur. Phys. J. B **91**, 170 (2018).

[24] T. Shimazaki and Y. Asai, Band structure calculations based on screened Fock exchange method, Chem. Phys. Lett. **466**, 91 (2008).

[25] L. Kronik and J. B. Neaton, Excited-state properties of molecular solids from first principles, Annu. Rev. Phys. Chem. **67**, 587 (2016).

[26] S. Refaely-Abramson, S. Sharifzadeh, M. Jain, R. Baer, J. B. Neaton, and L. Kronik, Gap renormalization of molecular crystals from density-functional theory, Phys. Rev. B **88**, 081204(R) (2013).

[27] S. Refaely-Abramson, M. Jain, S. Sharifzadeh, J. B. Neaton, and L. Kronik, Solid-state optical absorption from optimally tuned time-dependent range-separated hybrid density functional theory, Phys. Rev. B **92**, 081204(R) (2015).

[28] Z. Zheng, D. A. Egger, J.-L. Brédas, L. Kronik, and V. Coropceanu, Effect of solid-state polarization on charge-transfer excitations and transport levels at organic interfaces

from a screened range-separated hybrid functional, J. Phys. Chem. Lett. **8**, 3277 (2017).

[29] L. Kronik and S. Kümmel, Dielectric screening meets optimally tuned density functionals, Adv. Mater. **30**, 1706560 (2018).

[30] L. Kronik and S. Kümmel, Piecewise linearity, freedom from self-interaction, and a Coulomb asymptotic potential: Three related yet inequivalent properties of the exact density functional, Phys. Chem. Chem. Phys. **22**, 16467 (2020).

[31] M. Gerosa, C. E. Bottani, L. Caramella, G. Onida, C. Di Valentin, and G. Pacchioni, Electronic structure and phase stability of oxide semiconductors: Performance of dielectric-dependent hybrid functional DFT, benchmarked against *GW* band structure calculations and experiments, Phys. Rev. B **91**, 155201 (2015).

[32] A. Tal, P. Liu, G. Kresse, and A. Pasquarello, Accurate optical spectra through time-dependent density functional theory based on screening-dependent hybrid functionals, Phys. Rev. Res. **2**, 032019(R) (2020).

[33] Z.-h. Yang, F. Sottile, and C. A. Ullrich, Simple screened exact-exchange approach for excitonic properties in solids, Phys. Rev. B **92**, 035202 (2015).

[34] J. Sun, J. Yang, and C. A. Ullrich, Low-cost alternatives to the Bethe-Salpeter equation: Towards simple hybrid functionals for excitonic effects in solids, Phys. Rev. Res. **2**, 013091 (2020).

[35] J. Sun and C. A. Ullrich, Optical properties of $CsCu_2X_3$(X = Cl, Br, and I): A comparative study between hybrid time-dependent density-functional theory and the Bethe-Salpeter equation, Phys. Rev. Mater. **4**, 095402 (2020).

[36] W. Chen, G. Miceli, G.-M. Rignanese, and A. Pasquarello, Nonempirical dielectric-dependent hybrid functional with range separation for semiconductors and insulators, Phys. Rev. Mater. **2**, 073803 (2018).

[37] D. Wing, J. B. Haber, R. Noff, B. Barker, D. A. Egger, A. Ramasubramaniam, S. G. Louie, J. B. Neaton, and L. Kronik, Comparing time-dependent density functional theory with many-body perturbation theory for semiconductors: Screened range-separated hybrids and the *GW* plus Bethe-Salpeter approach, Phys. Rev. Mater. **3**, 064603 (2019).

[38] A. Ramasubramaniam, D. Wing, and L. Kronik, Transferable screened range-separated hybrids for layered materials: The cases of MoS_2 and H-Bn, Phys. Rev. Mater. **3**, 084007 (2019).

[39] D. Wing, J. B. Neaton, and L. Kronik, Time-dependent density functional theory of narrow band gap semiconductors using a screened range-separated hybrid functional, Adv. Theory Simul. **3**, 2000220 (2020).

[40] D. K. Lewis, A. Ramasubramaniam, and S. Sharifzadeh, Tuned and screened range-separated hybrid density functional theory for describing electronic and optical properties of defective gallium nitride, Phys. Rev. Mater. **4**, 063803 (2020).

[41] M. Camarasa-Gómez, A. Ramasubramaniam, J. B. Neaton, and L. Kronik, Transferable screened range-separated hybrid functionals for electronic and optical properties of van der Waals materials, Phys. Rev. Mater. **7**, 104001 (2023).

[42] D. Wing, G. Ohad, J. B. Haber, M. R. Filip, S. E. Gant, J. B. Neaton, and L. Kronik, Band gaps of crystalline solids from Wannier-localization–based optimal tuning of a screened range-separated hybrid functional, Proc. Natl. Acad. Sci. USA **118**, e2104556118 (2021).

[43] J. Ma and L.-W. Wang, Using Wannier functions to improve solid band gap predictions in density functional theory, Sci. Rep. **6**, 24924 (2016).

[44] G. Ohad, D. Wing, S. E. Gant, A. V. Cohen, J. B. Haber, F. Sagredo, M. R. Filip, J. B. Neaton, and L. Kronik, Band gaps of halide perovskites from a Wannier-localized optimally tuned screened range-separated hybrid functional, Phys. Rev. Mater. **6**, 104606 (2022).

[45] S. E. Gant, J. B. Haber, M. R. Filip, F. Sagredo, D. Wing, G. Ohad, L. Kronik, and J. B. Neaton, Optimally tuned starting point for single-shot GW calculations of solids, Phys. Rev. Mater. **6**, 053802 (2022).

[46] J. L. G. Fierro, *Metal Oxides: Chemistry and Applications* (CRC Press, Boca Raton, 2005).

[47] X. Yu, T. J. Marks, and A. Facchetti, Metal oxides for optoelectronic applications, Nat. Mater. **15**, 383 (2016).

[48] T. Das, G. Di Liberto, S. Tosoni, and G. Pacchioni, Band gap of 3D metal oxides and quasi-2D materials from hybrid density functional theory: Are dielectric-dependent functionals superior? J. Chem. Theory Comput. **15**, 6294 (2019).

[49] M. Gerosa, C. Bottani, C. Di Valentin, G. Onida, and G. Pacchioni, Accuracy of dielectric-dependent hybrid functionals in the prediction of optoelectronic properties of metal oxide semiconductors: A comprehensive comparison with many-body GW and experiments, J. Phys.: Condens. Matter **30**, 044003 (2018).

[50] V. L. Chevrier, S. P. Ong, R. Armiento, M. K. Chan, and G. Ceder, Hybrid density functional calculations of redox potentials and formation energies of transition metal compounds, Phys. Rev. B **82**, 075122 (2010).

[51] W. Li, C. F. Walther, A. Kuc, and T. Heine, Density functional theory and beyond for band-gap screening: Performance for transition-metal oxides and dichalcogenides, J. Chem. Theory Comput. **9**, 2950 (2013).

[52] P. Liu, C. Franchini, M. Marsman, and G. Kresse, Assessing model-dielectric-dependent hybrid functionals on the antiferromagnetic transition-metal monoxides MnO, FeO, CoO, and NiO, J. Phys.: Condens. Matter **32**, 015502 (2020).

[53] S. Mandal, K. Haule, K. M. Rabe, and D. Vanderbilt, Systematic beyond-DFT study of binary transition metal oxides, npj Comput. Mater. **5**, 115 (2019).

[54] S. Massidda, A. Continenza, M. Posternak, and A. Baldereschi, Quasiparticle energy bands of transition-metal oxides within a model GW scheme, Phys. Rev. B **55**, 13494 (1997).

[55] I. Østrøm, M. A. Hossain, P. A. Burr, J. N. Hart, and B. Hoex, Designing 3D metal oxides: Selecting optimal density functionals for strongly correlated materials, Phys. Chem. Chem. Phys. **24**, 14119 (2022).

[56] G. Samsonidze, C.-H. Park, and B. Kozinsky, Insights and challenges of applying the GW method to transition metal oxides, J. Phys.: Condens. Matter **26**, 475501 (2014).

[57] M. Weng, F. Pan, and L.-W. Wang, Wannier–Koopmans method calculations for transition metal oxide band gaps, npj Comput. Mater. **6**, 33 (2020).

[58] J. E. Coulter, E. Manousakis, and A. Gali, Limitations of the hybrid functional approach to electronic structure of transition metal oxides, Phys. Rev. B **88**, 041107(R) (2013).

[59] B.-C. Shih, Y. Xue, P. Zhang, M. L. Cohen, and S. G. Louie, Quasiparticle band gap of ZnO: High accuracy from the

conventional G^0W^0 approach, Phys. Rev. Lett. **105**, 146401 (2010).
[60] F. Bruneval, N. Vast, L. Reining, M. Izquierdo, F. Sirotti, and N. Barrett, Exchange and correlation effects in electronic excitations of Cu_2O, Phys. Rev. Lett. **97**, 267601 (2006).
[61] W. Kang and M. S. Hybertsen, Quasiparticle and optical properties of rutile and anatase TiO_2, Phys. Rev. B **82**, 085203 (2010).
[62] M. Shishkin and G. Kresse, Self-consistent *GW* calculations for semiconductors and insulators, Phys. Rev. B **75**, 235102 (2007).
[63] M. van Schilfgaarde, T. Kotani, and S. Faleev, Quasiparticle Self-Consistent *GW* Theory, Phys. Rev. Lett. **96**, 226402 (2006).
[64] T. Rangel, M. Del Ben, D. Varsano, G. Antonius, F. Bruneval, F. H. da Jornada, M. J. van Setten, O. K. Orhan, D. D. O'Regan, A. Canning, A. Ferretti, A. Marini, G.-M. Rignanese, J. Deslippe, S. G. Louie, and J. B. Neaton, Reproducibility in G_0W_0 calculations for solids, Comput. Phys. Commun. **255**, 107242 (2020).
[65] A. Schleife, F. Fuchs, C. Rödl, J. Furthmüller, and F. Bechstedt, Band-structure and optical-transition parameters of wurtzite MgO, ZnO, and CdO from quasiparticle calculations, Phys. Status Solidi B **246**, 2150 (2009).
[66] D. Golze, M. Dvorak, and P. Rinke, The GW compendium: A practical guide to theoretical photoemission spectroscopy, Front. Chem. **7**, 377 (2019).
[67] Y.-N. Wu, W. A. Saidi, P. Ohodnicki, B. Chorpening, and Y. Duan, First-principles investigations of the temperature dependence of electronic structure and optical properties of rutile TiO_2, J. Phys. Chem. C **122**, 22642 (2018).
[68] Y.-N. Wu, J. K. Wuenschell, R. Fryer, W. A. Saidi, P. Ohodnicki, B. Chorpening, and Y. Duan, Theoretical and experimental study of temperature effect on electronic and optical properties of TiO_2: Comparing rutile and anatase, J. Phys.: Condens. Matter **32**, 405705 (2020).
[69] J. Park, W. A. Saidi, B. Chorpening, and Y. Duan, Applicability of Allen–Heine–Cardona theory on MO_X metal oxides and ABO_3 perovskites: Toward high-temperature optoelectronic applications, Chem. Mater. **34**, 6108 (2022).
[70] J. P. Perdew and A. Zunger, Self-interaction correction to density-functional approximations for many-electron systems, Phys. Rev. B **23**, 5048 (1981).
[71] P. Mori-Sánchez, A. J. Cohen, and W. Yang, Localization and delocalization errors in density functional theory and implications for band-gap prediction, Phys. Rev. Lett. **100**, 146401 (2008).
[72] W. Aggoune, A. Eljarrat, D. Nabok, K. Irmscher, M. Zupancic, Z. Galazka, M. Albrecht, C. Koch, and C. Draxl, A consistent picture of excitations in cubic $BaSnO_3$ revealed by combining theory and experiment, Commun. Mater. **3**, 12 (2022).
[73] J. Wiktor, I. Reshetnyak, F. Ambrosio, and A. Pasquarello, Comprehensive modeling of the band gap and absorption spectrum of $BiVO_4$, Phys. Rev. Mater. **1**, 022401(R) (2017).
[74] O. Madelung, *Semiconductors Data Handbook*, 3rd ed. (Springer-Verlag Berlin Heidelberg, 2004).
[75] S. Kondo, K. Tateishi, and N. Ishizawa, Structural evolution of corundum at high temperatures, Jpn. J. Appl. Phys. **47**, 616 (2008).
[76] K. Sugiyama and Y. Takeuchi, The crystal structure of rutile as a function of temperature up to 1600°C, Z. Kristallogr. - Cryst. Mater. **194**, 305 (1991).
[77] M. L. Foo, Q. Huang, J. Lynn, W.-L. Lee, T. Klimczuk, I. Hagemann, N. Ong, and R. J. Cava, Synthesis, structure and physical properties of Ru ferrites: $BaMRu_5O_{11}$ (M = Li and Cu) and $BaM'_2Ru_4O_{11}$ (M' = Mn, Fe, and Co), J. Solid State Chem. **179**, 563 (2006).
[78] O. Garcia-Martinez, R. Rojas, E. Vila, and J. M. De Vidales, Microstructural characterization of nanocrystals of ZnO and CuO obtained from basic salts, Solid State Ionics **63-65**, 442 (1993).
[79] H. Mizoguchi, P. M. Woodward, C.-H. Park, and D. A. Keszler, Strong near-infrared luminescence in $BaSnO_3$, J. Am. Chem. Soc. **126**, 9796 (2004).
[80] A. Sleight, H.-Y. Chen, A. Ferretti, and D. Cox, Crystal growth and structure of $BiVO_4$, Mater. Res. Bull. **14**, 1571 (1979).
[81] J. P. Perdew, K. Burke, and M. Ernzerhof, Generalized gradient approximation made simple, Phys. Rev. Lett. **77**, 3865 (1996).
[82] J. P. Perdew, M. Ernzerhof, and K. Burke, Rationale for mixing exact exchange with density functional approximations, J. Chem. Phys. **105**, 9982 (1996).
[83] C. Adamo and V. Barone, Toward reliable density functional methods without adjustable parameters: The PBE0 model, J. Chem. Phys. **110**, 6158 (1999).
[84] J. Heyd, G. E. Scuseria, and M. Ernzerhof, Erratum: "Hybrid functionals based on a screened Coulomb potential" [J. Chem. Phys. **118**, 8207 (2003)], J. Chem. Phys. **124**, 219906 (2006).
[85] J. P. Perdew, R. G. Parr, M. Levy, and J. L. Balduz, Density-functional theory for fractional particle number: Derivative discontinuities of the energy, Phys. Rev. Lett. **49**, 1691 (1982).
[86] C.-O. Almbladh and U. von Barth, Exact results for the charge and spin densities, exchange-correlation potentials, and density-functional eigenvalues, Phys. Rev. B **31**, 3231 (1985).
[87] J. P. Perdew and M. Levy, Comment on "Significance of the highest occupied Kohn-Sham eigenvalue," Phys. Rev. B **56**, 16021 (1997).
[88] M. Levy, J. P. Perdew, and V. Sahni, Exact differential equation for the density and ionization energy of a many-particle system, Phys. Rev. A **30**, 2745 (1984).
[89] T. Stein, H. Eisenberg, L. Kronik, and R. Baer, Fundamental gaps in finite systems from eigenvalues of a generalized Kohn-Sham method, Phys. Rev. Lett. **105**, 266802 (2010).
[90] L. Kronik, T. Stein, S. Refaely-Abramson, and R. Baer, Excitation gaps of finite-sized systems from optimally tuned range-separated hybrid functionals, J. Chem. Theory Comput. **8**, 1515 (2012).
[91] S. Refaely-Abramson, R. Baer, and L. Kronik, Fundamental and excitation gaps in molecules of relevance for organic photovoltaics from an optimally tuned range-separated hybrid functional, Phys. Rev. B **84**, 075144 (2011).
[92] J. Autschbach and M. Srebro, Delocalization error and "functional tuning" in Kohn–Sham calculations of molecular properties, Acc. Chem. Res. **47**, 2592 (2014).
[93] H. Phillips, Z. Zheng, E. Geva, and B. D. Dunietz, Orbital gap predictions for rational design of organic photovoltaic materials, Org. Electron. **15**, 1509 (2014).

[94] M. E. Foster, J. D. Azoulay, B. M. Wong, and M. D. Allendorf, Novel metal–organic framework linkers for light harvesting applications, Chem. Sci. **5**, 2081 (2014).
[95] T. Körzdörfer and J.-L. Brédas, Organic electronic materials: Recent advances in the DFT description of the ground and excited states using tuned range-separated hybrid functionals, Acc. Chem. Res. **47**, 3284 (2014).
[96] C. Faber, P. Boulanger, C. Attaccalite, I. Duchemin, and X. Blase, Excited states properties of organic molecules: From density functional theory to the GW and Bethe–Salpeter Green's function formalisms, Philos. Trans. R. Soc. London, Ser. A **372**, 20130271 (2014).
[97] E. Kraisler and L. Kronik, Fundamental gaps with approximate density functionals: The derivative discontinuity revealed from ensemble considerations, J. Chem. Phys. **140**, 18A540 (2014).
[98] V. Vlček, H. R. Eisenberg, G. Steinle-Neumann, L. Kronik, and R. Baer, Deviations from piecewise linearity in the solid-state limit with approximate density functionals, J. Chem. Phys. **142**, 034107 (2015).
[99] A. Görling, Exchange-correlation potentials with proper discontinuities for physically meaningful Kohn-Sham eigenvalues and band structures, Phys. Rev. B **91**, 245120 (2015).
[100] V. I. Anisimov and A. V. Kozhevnikov, Transition state method and Wannier functions, Phys. Rev. B **72**, 075125 (2005).
[101] M. Weng, S. Li, J. Ma, J. Zheng, F. Pan, and L.-W. Wang, Wannier Koopman method calculations of the band gaps of alkali halides, Appl. Phys. Lett. **111**, 054101 (2017).
[102] C. Li, X. Zheng, N. Q. Su, and W. Yang, Localized orbital scaling correction for systematic elimination of delocalization error in density functional approximations, Natl. Sci. Rev. **5**, 203 (2018).
[103] G. Miceli, W. Chen, I. Reshetnyak, and A. Pasquarello, Nonempirical hybrid functionals for band gaps and polaronic distortions in solids, Phys. Rev. B **97**, 121112 (2018).
[104] N. L. Nguyen, N. Colonna, A. Ferretti, and N. Marzari, Koopmans-compliant spectral functionals for extended systems, Phys. Rev. X **8**, 021051 (2018).
[105] T. Bischoff, I. Reshetnyak, and A. Pasquarello, Adjustable potential probes for band-gap predictions of extended systems through nonempirical hybrid functionals, Phys. Rev. B **99**, 201114 (2019).
[106] T. Bischoff, J. Wiktor, W. Chen, and A. Pasquarello, Nonempirical hybrid functionals for band gaps of inorganic metal-halide perovskites, Phys. Rev. Mater. **3**, 123802 (2019).
[107] J. D. Elliott, N. Colonna, M. Marsili, N. Marzari, and P. Umari, Koopmans meets Bethe–Salpeter: Excitonic optical spectra without GW, J. Chem. Theory Comput. **15**, 3710 (2019).
[108] N. Q. Su, A. Mahler, and W. Yang, Preserving symmetry and degeneracy in the localized orbital scaling correction approach, J. Phys. Chem. Lett. **11**, 1528 (2020).
[109] T. Bischoff, I. Reshetnyak, and A. Pasquarello, Band gaps of liquid water and hexagonal ice through advanced electronic-structure calculations, Phys. Rev. Res. **3**, 023182 (2021).
[110] N. Colonna, R. De Gennaro, E. Linscott, and N. Marzari, Koopmans spectral functionals in periodic boundary conditions, J. Chem. Theory Comput. **18**, 5435 (2022).
[111] A. Mahler, J. Williams, N. Q. Su, and W. Yang, Localized orbital scaling correction for periodic systems, Phys. Rev. B **106**, 035147 (2022).
[112] J. Yang, S. Falletta, and A. Pasquarello, One-shot approach for enforcing piecewise linearity on hybrid functionals: Application to band gap predictions, J. Phys. Chem. Lett. **13**, 3066 (2022).
[113] R. De Gennaro, N. Colonna, E. Linscott, and N. Marzari, Bloch's theorem in orbital-density-dependent functionals: Band structures from Koopmans spectral functionals, Phys. Rev. B **106**, 035106 (2022).
[114] E. B. Linscott, N. Colonna, R. De Gennaro, N. L. Nguyen, G. Borghi, A. Ferretti, I. Dabo, and N. Marzari, Koopmans: An open-source package for accurately and efficiently predicting spectral properties with Koopmans functionals, J. Chem. Theory Comput. **19**, 7097 (2023).
[115] See Supplemental Material at http://link.aps.org/supplemental/10.1103/PhysRevMaterials.7.123803 for more computational details and further analysis, which includes Refs. [186–204].
[116] S. Hirata and M. Head-Gordon, Time-dependent density functional theory within the Tamm–Dancoff approximation, Chem. Phys. Lett. **314**, 291 (1999).
[117] H.-Y. Sun, S.-X. Li, and H. Jiang, Pros and cons of the time-dependent hybrid density functional approach for calculating the optical spectra of solids: A case study of CeO_2, Phys. Chem. Chem. Phys. **23**, 16296 (2021).
[118] W. Luo, S. Ismail-Beigi, M. L. Cohen, and S. G. Louie, Quasiparticle band structure of ZnS and ZnSe, Phys. Rev. B **66**, 195215 (2002).
[119] S. V. Faleev, M. van Schilfgaarde, and T. Kotani, All-electron self-consistent *GW* approximation: Application to Si, MnO, and NiO, Phys. Rev. Lett. **93**, 126406 (2004).
[120] T. Kotani, M. van Schilfgaarde, and S. V. Faleev, Quasiparticle self-consistent *GW* method: A basis for the independent-particle approximation, Phys. Rev. B **76**, 165106 (2007).
[121] M. S. Hybertsen and S. G. Louie, First-principles theory of quasiparticles: Calculation of band gaps in semiconductors and insulators, Phys. Rev. Lett. **55**, 1418 (1985).
[122] S. L. Adler, Quantum theory of the dielectric constant in real solids, Phys. Rev. **126**, 413 (1962).
[123] N. Wiser, Dielectric constant with local field effects included, Phys. Rev. **129**, 62 (1963).
[124] R. W. Godby, M. Schlüter, and L. J. Sham, Self-energy operators and exchange-correlation potentials in semiconductors, Phys. Rev. B **37**, 10159 (1988).
[125] M. Govoni and G. Galli, Large scale GW calculations, J. Chem. Theory Comput. **11**, 2680 (2015).
[126] H.-V. Nguyen, T. A. Pham, D. Rocca, and G. Galli, Improving accuracy and efficiency of calculations of photoemission spectra within the many-body perturbation theory, Phys. Rev. B **85**, 081101 (2012).
[127] T. A. Pham, H.-V. Nguyen, D. Rocca, and G. Galli, GW calculations using the spectral decomposition of the dielectric matrix: Verification, validation, and comparison of methods, Phys. Rev. B **87**, 155148 (2013).
[128] H. F. Wilson, F. Gygi, and G. Galli, Efficient iterative method for calculations of dielectric matrices, Phys. Rev. B **78**, 113303 (2008).
[129] H. F. Wilson, D. Lu, F. Gygi, and G. Galli, Iterative calcula-

tions of dielectric eigenvalue spectra, Phys. Rev. B **79**, 245106 (2009).

[130] M. Del Ben, F. H. da Jornada, G. Antonius, T. Rangel, S. G. Louie, J. Deslippe, and A. Canning, Static subspace approximation for the evaluation of G_0W_0 quasiparticle energies within a sum-over-bands approach, Phys. Rev. B **99**, 125128 (2019).

[131] R. W. Godby and R. J. Needs, Metal-insulator transition in Kohn-Sham theory and quasiparticle theory, Phys. Rev. Lett. **62**, 1169 (1989).

[132] A. Oschlies, R. W. Godby, and R. J. Needs, GW self-energy calculations of carrier-induced band-gap narrowing in n-type silicon, Phys. Rev. B **51**, 1527 (1995).

[133] M. Giantomassi, M. Stankovski, R. Shaltaf, M. Grüning, F. Bruneval, P. Rinke, and G.-M. Rignanese, Electronic properties of interfaces and defects from many-body perturbation theory: Recent developments and applications, Phys. Status Solidi B **248**, 275 (2011).

[134] P. Liu, M. Kaltak, J. Klimeš, and G. Kresse, Cubic scaling GW: Towards fast quasiparticle calculations, Phys. Rev. B **94**, 165109 (2016).

[135] J. Wilhelm, M. Del Ben, and J. Hutter, GW in the Gaussian and plane waves scheme with application to linear acenes, J. Chem. Theory Comput. **12**, 3623 (2016).

[136] W. G. Aulbur, L. Jönsson, and J. W. Wilkins, Quasiparticle calculations in solids, in *Solid State Physics*, Vol. 54, edited by H. Ehrenreich and F. Spaepen (Academic Press, New York, 2000), pp. 1–218.

[137] S. G. Louie and A. Rubio, Quasiparticle and optical properties of solids and nanostructures: The GW-BSE approach, in *Handbook of Materials Modeling* (Springer, New York, 2005), pp. 215–240.

[138] F. Fuchs, J. Furthmüller, F. Bechstedt, M. Shishkin, and G. Kresse, Quasiparticle band structure based on a generalized Kohn-Sham scheme, Phys. Rev. B **76**, 115109 (2007).

[139] W. Chen and A. Pasquarello, Accurate band gaps of extended systems via efficient vertex corrections in GW, Phys. Rev. B **92**, 041115(R) (2015).

[140] H. Jiang and P. Blaha, GW with linearized augmented plane waves extended by high-energy local orbitals, Phys. Rev. B **93**, 115203 (2016).

[141] M. Grumet, P. Liu, M. Kaltak, J. Klimeš, and G. Kresse, Beyond the quasiparticle approximation: Fully self-consistent GW calculations, Phys. Rev. B **98**, 155143 (2018).

[142] P. Rinke, A. Qteish, J. Neugebauer, C. Freysoldt, and M. Scheffler, Combining GW calculations with exact-exchange density-functional theory: An analysis of valence-band photoemission for compound semiconductors, New J. Phys. **7**, 126 (2005).

[143] F. Bruneval and M. A. L. Marques, Benchmarking the starting points of the GW approximation for molecules, J. Chem. Theory Comput. **9**, 324 (2013).

[144] M. J. van Setten, M. Giantomassi, X. Gonze, G.-M. Rignanese, and G. Hautier, Automation methodologies and large-scale validation for GW: Towards high-throughput GW calculations, Phys. Rev. B **96**, 155207 (2017).

[145] L. Leppert, T. Rangel, and J. B. Neaton, Towards predictive band gaps for halide perovskites: Lessons from one-shot and eigenvalue self-consistent GW, Phys. Rev. Mater. **3**, 103803 (2019).

[146] N. Marom, F. Caruso, X. Ren, O. T. Hofmann, T. Körzdörfer, J. R. Chelikowsky, A. Rubio, M. Scheffler, and P. Rinke, Benchmark of GW methods for azabenzenes, Phys. Rev. B **86**, 245127 (2012).

[147] S. Sharifzadeh, Many-body perturbation theory for understanding optical excitations in organic molecules and solids, J. Phys.: Condens. Matter **30**, 153002 (2018).

[148] M. Rohlfing and S. G. Louie, Electron-hole excitations in semiconductors and insulators, Phys. Rev. Lett. **81**, 2312 (1998).

[149] J. Deslippe, G. Samsonidze, D. A. Strubbe, M. Jain, M. L. Cohen, and S. G. Louie, Berkeley GW: A massively parallel computer package for the calculation of the quasiparticle and optical properties of materials and nanostructures, Comput. Phys. Commun. **183**, 1269 (2012).

[150] T. Tomiki, Y. Ganaha, T. Futemma, T. Shikenbaru, Y. Aiura, M. Yuri, S. Sato, H. Fukutani, H. Kato, T. Miyahara *et al.*, Anisotropic optical spectra of α-Al_2O_3 single crystals in the vacuum ultraviolet region, II. Spectra of optical constants, J. Phys. Soc. Jpn. **62**, 1372 (1993).

[151] M. Bortz, R. French, D. Jones, R. Kasowski, and F. Ohuchi, Temperature dependence of the electronic structure of oxides: MgO, $MgAl_2O_4$, and Al_2O_3, Phys. Scr. **41**, 537 (1990).

[152] T. E. Tiwald and M. Schubert, Measurement of rutile TiO_2 dielectric tensor from 0.148 to 33 μm using generalized ellipsometry, in *Optical Diagnostic Methods For Inorganic Materials II*, Vol. 4103 (SPIE, Bellingham, WA, 2000), pp. 19–29.

[153] R. C. Whited and W. Walker, Exciton and interband spectra of crystalline CaO, Phys. Rev. **188**, 1380 (1969).

[154] P. Gori, M. Rakel, C. Cobet, W. Richter, N. Esser, A. Hoffmann, R. Del Sole, A. Cricenti, and O. Pulci, Optical spectra of ZnO in the far ultraviolet: First-principles calculations and ellipsometric measurements, Phys. Rev. B **81**, 125207 (2010).

[155] F. Haidu, M. Fronk, O. D. Gordan, C. Scarlat, G. Salvan, and D. R. Zahn, Dielectric function and magneto-optical Voigt constant of Cu_2O: A combined spectroscopic ellipsometry and polar magneto-optical Kerr spectroscopy study, Phys. Rev. B **84**, 195203 (2011).

[156] J. Wiktor, U. Rothlisberger, and A. Pasquarello, Predictive determination of band gaps of inorganic halide perovskites, J. Phys. Chem. Lett. **8**, 5507 (2017).

[157] H. Wang, A. Tal, T. Bischoff, P. Gono, and A. Pasquarello, Accurate and efficient band-gap predictions for metal halide perovskites at finite temperature, npj Comput. Mater. **8**, 237 (2022).

[158] F. Giustino, Electron-phonon interactions from first principles, Rev. Mod. Phys. **89**, 015003 (2017).

[159] F. Karsai, M. Engel, E. Flage-Larsen, and G. Kresse, Electron–phonon coupling in semiconductors within the GW approximation, New J. Phys. **20**, 123008 (2018).

[160] A. Miglio, V. Brousseau-Couture, E. Godbout, G. Antonius, Y.-H. Chan, S. G. Louie, M. Côté, M. Giantomassi, and X. Gonze, Predominance of non-adiabatic effects in zero-point renormalization of the electronic band gap, npj Comput. Mater. **6**, 167 (2020).

[161] G. Antonius and S. G. Louie, Theory of exciton-phonon coupling, Phys. Rev. B **105**, 085111 (2022).

[162] M. Engel, H. Miranda, L. Chaput, A. Togo, C. Verdi, M.

Marsman, and G. Kresse, Zero-point renormalization of the band gap of semiconductors and insulators using the projector augmented wave method, Phys. Rev. B **106**, 094316 (2022).
[163] M. Cardona and M. L. W. Thewalt, Isotope effects on the optical spectra of semiconductors, Rev. Mod. Phys. **77**, 1173 (2005).
[164] M. Zacharias and F. Giustino, One-shot calculation of temperature-dependent optical spectra and phonon-induced band-gap renormalization, Phys. Rev. B **94**, 075125 (2016).
[165] M. Zacharias and F. Giustino, Theory of the special displacement method for electronic structure calculations at finite temperature, Phys. Rev. Res. **2**, 013357 (2020).
[166] M. R. Filip, J. B. Haber, and J. B. Neaton, Phonon screening of excitons in semiconductors: Halide perovskites and beyond, Phys. Rev. Lett. **127**, 067401 (2021).
[167] D. Lüftner, S. Refaely-Abramson, M. Pachler, R. Resel, M. G. Ramsey, L. Kronik, and P. Puschnig, Experimental and theoretical electronic structure of quinacridone, Phys. Rev. B **90**, 075204 (2014).
[168] X. Blase, C. Attaccalite, and V. Olevano, First-principles GW calculations for fullerenes, porphyrins, phtalocyanine, and other molecules of interest for organic photovoltaic applications, Phys. Rev. B **83**, 115103 (2011).
[169] M. Usuda, N. Hamada, T. Kotani, and M. van Schilfgaarde, All-electron GW calculation based on the LAPW method: Application to wurtzite ZnO, Phys. Rev. B **66**, 125101 (2002).
[170] M. van Schilfgaarde, T. Kotani, and S. V. Faleev, Adequacy of approximations in *GW* theory, Phys. Rev. B **74**, 245125 (2006).
[171] M. Stankovski, G. Antonius, D. Waroquiers, A. Miglio, H. Dixit, K. Sankaran, M. Giantomassi, X. Gonze, M. Côté, and G.-M. Rignanese, G^0W^0 band gap of ZnO: Effects of plasmon-pole models, Phys. Rev. B **84**, 241201 (2011).
[172] C. Friedrich, M. Betzinger, M. Schlipf, S. Blügel, and A. Schindlmayr, Hybrid functionals and GW approximation in the FLAPW method, J. Phys.: Condens. Matter **24**, 293201 (2012).
[173] J. K. Cooper, S. Gul, F. M. Toma, L. Chen, Y.-S. Liu, J. Guo, J. W. Ager, J. Yano, and I. D. Sharp, Indirect bandgap and optical properties of monoclinic bismuth vanadate, J. Phys. Chem. C **119**, 2969 (2015).
[174] Y. Tezuka, S. Shin, T. Ishii, T. Ejima, S. Suzuki, and S. Sato, Photoemission and bremsstrahlung isochromat spectroscopy studies of TiO_2 (rutile) and $SrTiO_3$, J. Phys. Soc. Jpn. **63**, 347 (1994).
[175] R. Zimmermann, P. Steiner, R. Claessen, F. Reinert, S. Hüfner, P. Blaha, and P. Dufek, Electronic structure of 3D-transition-metal oxides: On-site Coulomb repulsion versus covalency, J. Phys.: Condens. Matter **11**, 1657 (1999).
[176] S. Sharifzadeh, A. Biller, L. Kronik, and J. B. Neaton, Quasiparticle and optical spectroscopy of the organic semiconductors pentacene and PTCDA from first principles, Phys. Rev. B **85**, 125307 (2012).
[177] R. C. Whited, C. J. Flaten, and W. Walker, Exciton thermoreflectance of MgO and CaO, Solid State Commun. **13**, 1903 (1973).
[178] R. H. French, Electronic band structure of Al_2O_3, with comparison to AlON and AIN, J. Am. Ceram. Soc. **73**, 477 (1990).
[179] J. Pascual, J. Camassel, and H. Mathieu, Resolved quadrupolar transition in TiO_2, Phys. Rev. Lett. **39**, 1490 (1977).
[180] M. Takahata and N. Naka, Photoluminescence properties of the entire excitonic series in Cu_2O, Phys. Rev. B **98**, 195205 (2018).
[181] S. Tsoi, X. Lu, A. Ramdas, H. Alawadhi, M. Grimsditch, M. Cardona, and R. Lauck, Isotopic-mass dependence of the a, b, and c excitonic band gaps in ZnO at low temperatures, Phys. Rev. B **74**, 165203 (2006).
[182] T. Kazimierczuk, D. Fröhlich, S. Scheel, H. Stolz, and M. Bayer, Giant Rydberg excitons in the copper oxide Cu_2O, Nature (London) **514**, 343 (2014).
[183] C. Uihlein, D. Fröhlich, and R. Kenklies, Investigation of exciton fine structure in Cu_2O, Phys. Rev. B **23**, 2731 (1981).
[184] T. J. Boerner, S. Deems, T. R. Furlani, S. L. Knuth, and J. Towns, ACCESS: Advancing Innovation: NSF's Advanced Cyberinfrastructure Coordination Ecosystem: Services & Support, *Practice and Experience in Advanced Research Computing*, PEARC '23 (Association for Computing Machinery, 2023), pp. 173–176.
[185] http://www.tacc.utexas.edu.
[186] G. Kresse and J. Furthmüller, Efficient iterative schemes for ab initio total-energy calculations using a plane-wave basis set, Phys. Rev. B **54**, 11169 (1996).
[187] G. Kresse and D. Joubert, From ultrasoft pseudopotentials to the projector augmented-wave method, Phys. Rev. B **59**, 1758 (1999).
[188] G. Makov and M. C. Payne, Periodic boundary conditions in ab initio calculations, Phys. Rev. B **51**, 4014 (1995).
[189] M. Leslie and N. J. Gillan, The energy and elastic dipole tensor of defects in ionic crystals calculated by the supercell method, J. Phys. C: Solid State Phys. **18**, 973 (1985).
[190] H.-P. Komsa, T. T. Rantala, and A. Pasquarello, Finite-size supercell correction schemes for charged defect calculations, Phys. Rev. B **86**, 045112 (2012).
[191] R. Rurali and X. Cartoixá, Theory of defects in one-dimensional systems: Application to Al-catalyzed Si nanowires, Nano Lett. **9**, 975 (2009).
[192] A. A. Mostofi, J. R. Yates, G. Pizzi, Y.-S. Lee, I. Souza, D. Vanderbilt, and N. Marzari, An updated version of Wannier90: A tool for obtaining maximally-localised Wannier functions, Comput. Phys. Commun. **185**, 2309 (2014).
[193] P. Giannozzi, S. Baroni, N. Bonini, M. Calandra, R. Car, C. Cavazzoni, D. Ceresoli, G. L. Chiarotti, M. Cococcioni, I. Dabo *et al.*, QUANTUM ESPRESSO: A modular and open-source software project for quantum simulations of materials, J. Phys.: Condens. Matter **21**, 395502 (2009).
[194] P. Giannozzi Jr., O. Andreussi, T. Brumme, O. Bunau, M. Buongiorno Nardelli, M. Calandra, R. Car, C. Cavazzoni, D. Ceresoli, M. Cococcioni *et al.*, Advanced capabilities for materials modelling with Quantum ESPRESSO, J. Phys.: Condens. Matter **29**, 465901 (2017).
[195] P. Giannozzi, O. Baseggio, P. Bonfà, D. Brunato, R. Car, I. Carnimeo, C. Cavazzoni, S. de Gironcoli, P. Delugas, F. Ferrari Ruffino *et al.*, Quantum ESPRESSO toward the exascale, J. Chem. Phys. **152**, 154105 (2020).
[196] D. R. Hamann, Optimized norm-conserving Vanderbilt pseudopotentials, Phys. Rev. B **88**, 085117 (2013).
[197] M. van Setten, M. Giantomassi, E. Bousquet, M. Verstraete, D. Hamann, X. Gonze, and G.-M. Rignanese, The PseudoDojo:

Training and grading a 85 element optimized norm-conserving pseudopotential table, Comput. Phys. Commun. **226**, 39 (2018).

[198] M. Rohlfing, P. Krüger, and J. Pollmann, Quasiparticle band structure of CdS, Phys. Rev. Lett. **75**, 3489 (1995).

[199] M. L. Tiago, S. Ismail-Beigi, and S. G. Louie, Effect of semicore orbitals on the electronic band gaps of Si, Ge, and GaAs within the GW approximation, Phys. Rev. B **69**, 125212 (2004).

[200] A. Fleszar and W. Hanke, Electronic structure of $\mathrm{II}^B - \mathrm{VI}$ semiconductors in the *GW* approximation, Phys. Rev. B **71**, 045207 (2005).

[201] P. Larson, M. Dvorak, and Z. Wu, Role of the plasmon-pole model in the *GW* approximation, Phys. Rev. B **88**, 125205 (2013).

[202] J. Deslippe, G. Samsonidze, M. Jain, M. L. Cohen, and S. G. Louie, Coulomb-hole summations and energies for *GW* calculations with limited number of empty orbitals: A modified static remainder approach, Phys. Rev. B **87**, 165124 (2013).

[203] S. Lany, Band-structure calculations for the 3d transition metal oxides in *GW*, Phys. Rev. B **87**, 085112 (2013).

[204] F. Bruneval, Exchange and correlation in the electronic structure of solids, from silicon to cuprous oxide: GW approximation and beyond, Ph.D. thesis, Ecole Polytechnique, 2005.